spatial and contrast resolution. However, because of the dual blood supply of the liver and intravenous injection of the contrast medium, the precise analysis of hemodynamics by conventional MDCT is often difficult. By the introduction of dynamic CT during selective arteriography, including CT during arterial portography (CTAP) [2, 3] and CT during hepatic arteriography (CTHA) [4], it has become possible to visualize the distribution of the intra-hepatic portal and arterial blood flow separately with extremely high contrast resolution, and as a result, to analyze precisely the correlation between blood supply and pathophysiology. In this article, blood flow imaging features of HCC will be discussed based on the CTAP and CTHA imaging and pathophysiologic correlations with special reference to multistep hepatocarcinogenesis.

Classification of hepatocellular nodules and multi-step hepatocarcinogenesis

The concept of multi-step hepatocarcinogenesis and related small hepatocellular nodules in the patients with chronic liver diseases, particularly those with cirrhosis or chronic hepatitis caused by hepatitis B or C viruses, was developed mainly in Japan. However, it had not been widely accepted throughout the world and the diagnostic criteria of these nodules different even among the world specialists. However, in 2009, the International Consensus Group for Hepatocellular Neoplasia organized by the world's leading liver pathologists finally reached agreement [5].

According to this report, these nodules are divided into large regenerative nodule, low grade DN (L-DN), high-grade DN (H-DN), and HCC. In addition, small HCC (less than 2 cm) is divided into early HCC and progressed HCC. Early HCC has a vaguely nodular appearance and is well differentiated. Progressed HCC has a distinctly nodular pattern and is mostly moderately differentiated, often with evidence of microvascular invasion. L-DNs are vaguely or distinct nodular with mild increase in cell density and no cytologic atypia. H-DNs are more likely to show a vaguely nodular pattern with architectural and/or cytologic atypia, but the atypia is insufficient for a diagnosis of HCC. They show increased cell density, sometimes more than two times higher than the surrounding nontumoral liver, often with an irregular trabecular pattern. Unpaired arteries are found in most lesions, but usually not in great numbers. A nodule with largely H-DN features containing a subnodule of well-differentiated HCC can be seen. Early HCCs are vaguely nodular and are characterized by various combinations of the following major histologic features; (1) increased cell density more than two times that of the surrounding tissue, with an increased nuclear/cytoplasm ratio and irregular thin-trabecular pattern; (2) varying numbers of portal tracts within the nodule (intratumoral portal tracts); (3) pseudoglandular pattern; (4) diffuse fatty change; and (5) varying numbers of unpaired arteries. Any of the features listed above may be diffused throughout the lesion or may be restricted to an expansile subnodule (nodule-in-nodule). Most importantly, because all of these features may also be found in H-DNs, it is important to note that stromal invasion remains most helpful in differentiating early HCC from H-DNs. However, the application of these criteria is challenging because most histologic criteria are arrayed on a gradual spectrum and cannot be easily summarized as present or absent.

Because of these reasons as described above, it should be realized that there must be various degree of overlaps among imaging features of these nodules and they may show gradual changes during multi-step hepatocarcinogenesis.

Angiogenesis during multi-step hepatocarcinogenesis

Vascular endothelial growth factor (VEGF) is known to play a critical role in the neovascularization in the development and progression of malignant neoplasms [6, 7]. VEGF is produced by tumor cells, and its binding with VEGF receptors such as Flt-1 and Flk-1, which are expressed on vascular endothelial cells, leads to the proliferation and migration of endothelial cells. In addition, VEGF receptors expressed on tumor cells are involved in tumor proliferation in an autocrine loop via interaction with VEGF produced by the tumor cells themselves [7]. Park et al. [8] reported that the expression of VEGF was correlated with angiogenesis and cell proliferation in hepatocarcinogenesis. On the other hand, tumors often encounter hypoxic conditions during their growth. Under such conditions, hypoxia inducible factor-1α (HIF-1α) promotes the transcriptional activity of angiogenesis-related molecules such as VEGF and erythropoietin by affecting the hypoxia response element and HIF-1α located in nuclei [7].

We analyzed these changes of the angiogenesis during multi-step hepatocarcinogenesis by immunohistochemical and molecular studies [7]. According to our analysis, it was found that hepatocellular areas around the portal tracts in DNs, including those with sinusoidal capillarization and unpaired arteries, were strongly positive for HIF-1α, whereas this molecule was faintly expressed in the surrounding livers. Cytoplasmic overexpression and intranuclear expression of HIF-1α, a more increased expression pattern, were also observed in HCC, suggesting that cytoplasmic HIF-1α might have been moved into the nuclei in activated HCC cells. HIF-1α is involved in the upregulation of genes harboring the hypoxia response element such as VEGF, suggesting that increased expression of HIF-1α in the areas around the portal tracts of DNs may be responsible for increased expression of

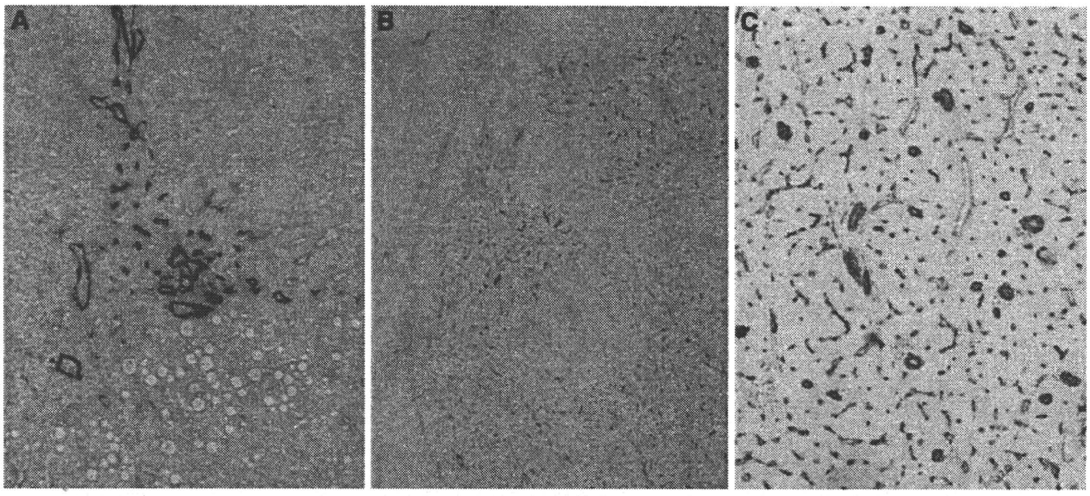

Fig. 1. Angiogenesis during multi-step hepatocarcinogenesis. Sinusoidal capillarization and unpaired arteries are expressed from spotty in DN (**A**, ×100), diffuse in early hepatocellular carcinoma (HCC) (**B**, ×50) to intense distribution in moderately differentiated HCC (**C**, ×100) in accordance with the elevation of the grade of malignancy of the nodules during hepatocarcinogenesis [Double immunohistochemical staining for CD 34 (*blue*) and α-smooth muscle actin (SMA) (*brown*)].

Fig. 2. Early HCC (high-grade DN with a well-differentiated HCC focus). **A** CT during hepatic arteriography (CTHA) shows entirely hypodense nodule (*arrow b*) with a slightly hyperdense focus (*arrow c*). **B** Double immunohistochemical staining for CD34 and αSMA of DN portion (*arrow b* in **A**) shows no definite expression of sinusoidal capillarization and unpaired arteries. **C** Double immunohistochemical staining of HCC portion corresponding (*arrow c* in **A**) shows expression of sinusoidal capillarization and unpaired arteries.

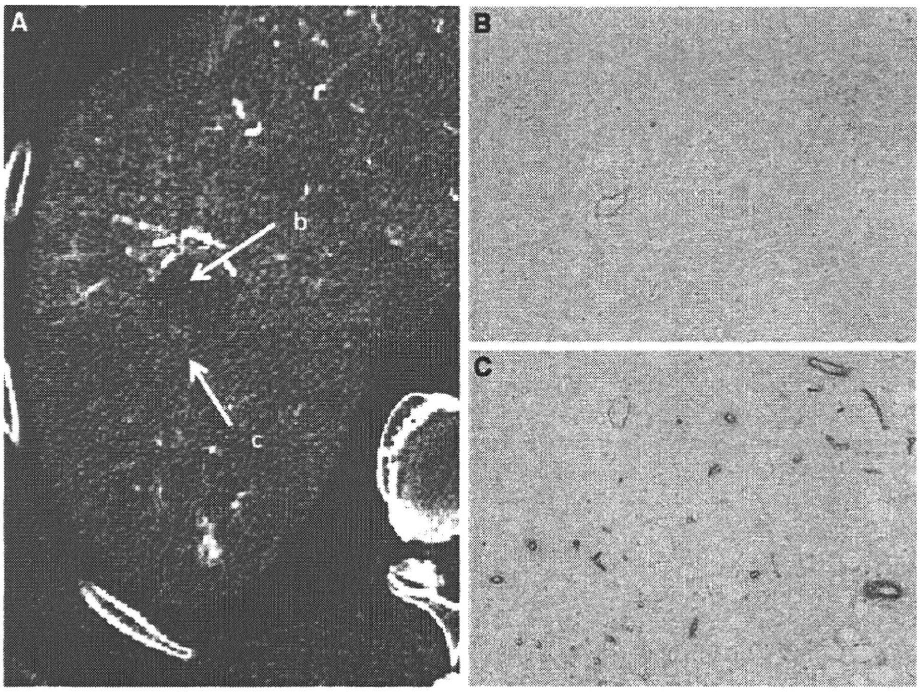

VEGF and its receptor followed by sinusoidal capillarization and increased numbers of unpaired arteries in DNs and also in the angiogenesis in HCC. These expressions gradually spread into the entire nodule in accordance with the elevation of the grade of malignancy of the nodules (Fig. 1).

Figure 2 shows an early HCC consisting of H-DN with a small part of highly differentiated HCC with stromal invasion. On CTHA, a well-differentiated focus demonstrates a faint enhancement and this portion reveals more expression of sinusoidal capillarization and unpaired arteries than that in the surrounding H-DN.

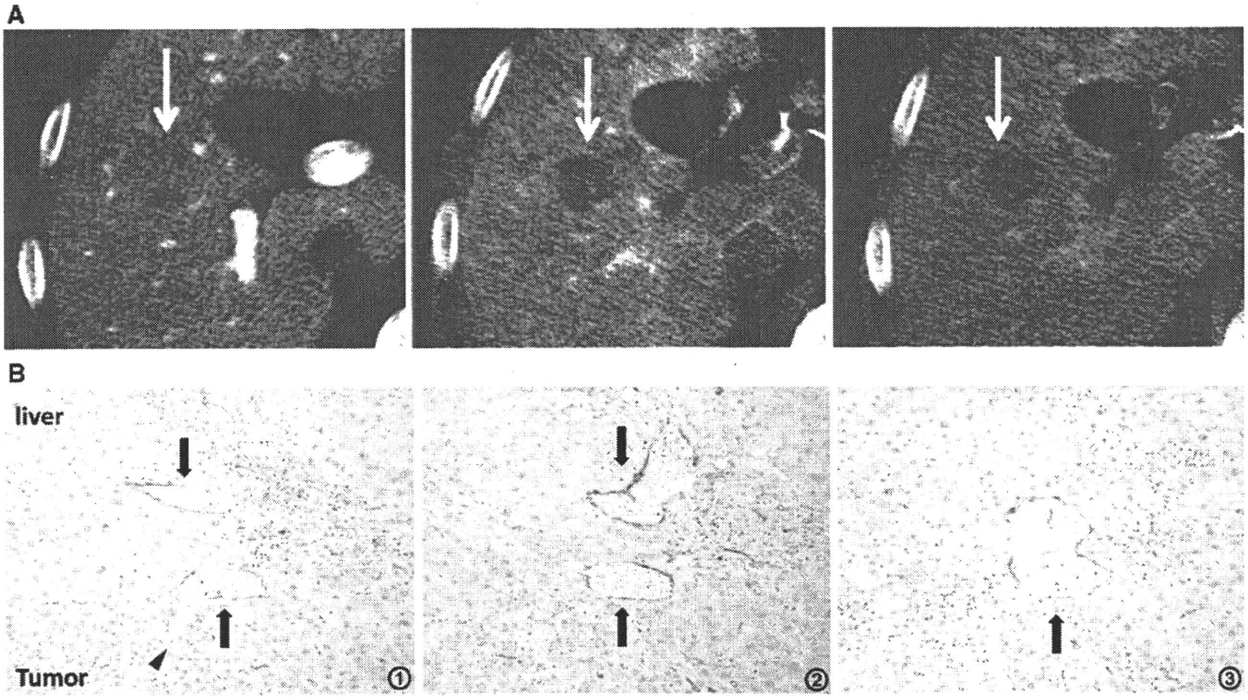

Fig. 3. High-grade DN. **A** Early phase of CTHA shows a hypodense nodule (*middle arrow*). It demonstrates isodensity on CT during arterial portography (CTAP, *left arrow*) and no perilesional enhancement on late phase of CTHA (*right arrow*). **B** Serial specimens from *1* to *3* with double immunohistochemical staining for CD 34 and α-SMA show the communication between intratumoral blood sinusoids (*arrowhead*) and hepatic venules (*arrows*) in the tumor (×100).

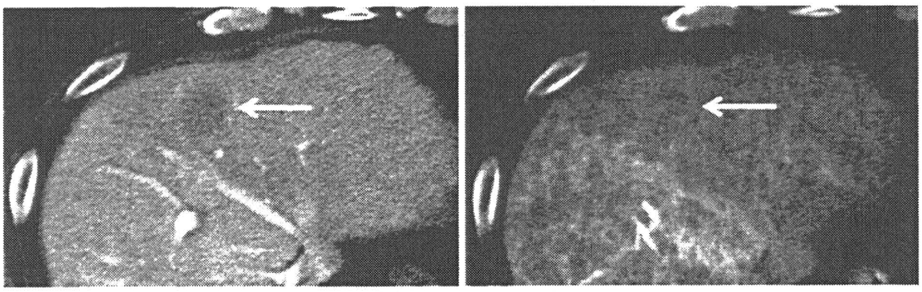

Fig. 4. Early HCC. CTAP (*left*) shows a faintly hypodense nodule indicating decreased but not absent intranodular portal supply (*arrow*). On CTHA (*right*), it is not well identified indicating almost the same intranodular arterial supply relative to the surrounding liver (*arrow*).

This case may indicate the gradual increase of angiogenesis during multi-step hepatocarcinogenesis.

Multi-step changes of intranodular blood supply during hepatocarcinogenesis

We previously described that the intranodular blood supply evaluated by CTAP and CTHA changed in accordance with hepatocarcinogenesis from DN to overt HCC [4, 9]. On CTAP, the intranodular portal supply could be divided into four types relative to the surrounding cirrhotic liver [4] (Figs. 3, 4, 5, 6, 7), namely, isodense nodule relative to the surrounding liver indicating almost the same intranodular portal supply (type A), slightly hypodense nodule indicating decreased but not absent intranodular portal blood flow (type B), a part of the nodule showing a definitely hypodense area indicating a partially absent intranodular portal blood supply (type C) and definitely hypodense indicating an absent intranodular portal supply (type D). The correlation between the histologic types of nodules and these CTAP findings revealed the significant correlation or

Fig. 5. Well-differentiated HCC (early HCC with subfocus of definite hypervascular well-differentiated HCC). CTAP (*left*) shows a slightly hypodense nodule with an internal definitely hypodense focus indicating partial portal perfusion defect (*arrow*). On CTHA (*right*), it is visualized as an entirely isodense nodule with an internal definitely hypervascular focus (*arrow*).

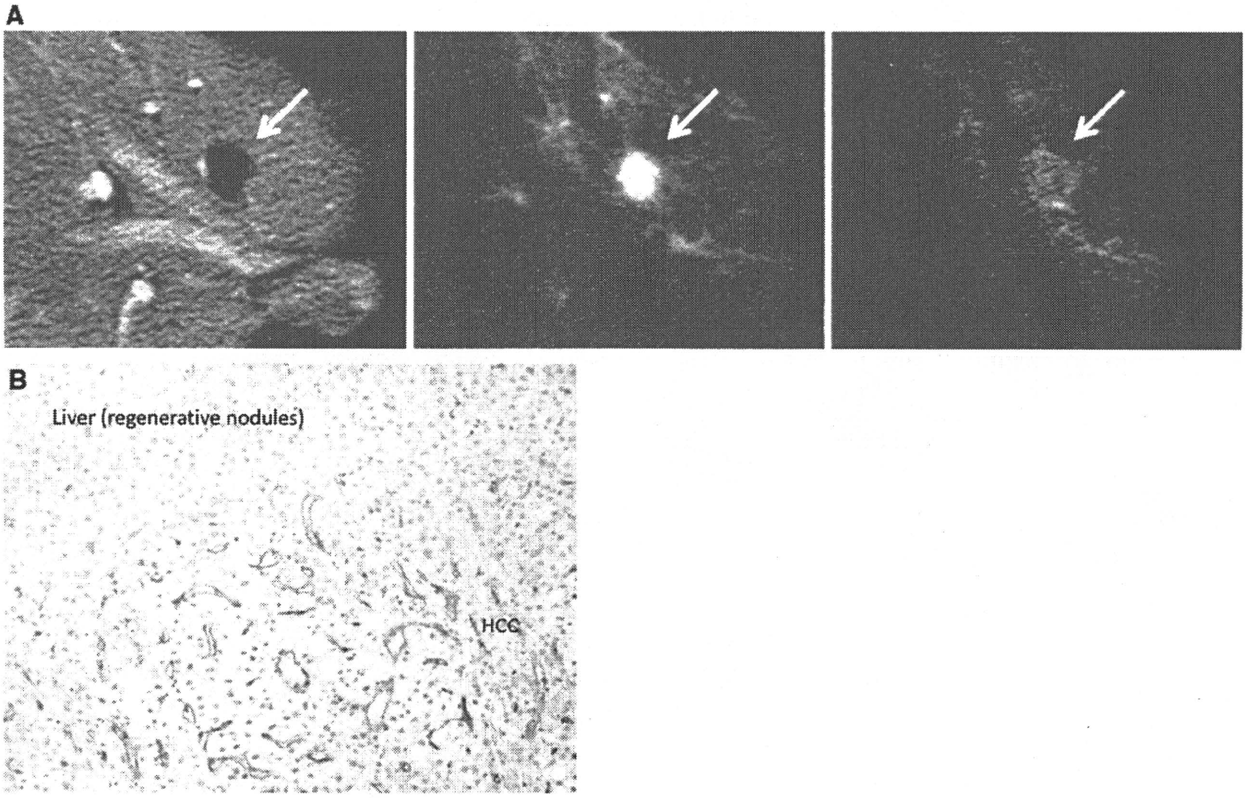

Fig. 6. Hypervascular well-differentiated HCC. **A** CTAP (*left*) shows an entirely hypodense nodule (*arrow*). It demonstrates hyperdensity on early phase of CTHA (*middle, arrow*) and thin corona enhancement on late phase of CTHA (*right, arrow*). **B** Double immunohistochemical staining of the boundary between the tumor and liver parenchyma shows abundant communications between intratumoral blood sinusoids and hepatic sinusoids (×100).

strong tendency between DN and type A, early HCC and type B, well-differentiated HCC and type C, and moderately or poorly differentiated HCC and type D (Figs. 3, 4, 5, 6, 7). On CTHA, the intranodular arterial supply could be also categorized into four types relative to the surrounding cirrhotic liver (Figs. 3, 4, 5, 6, 7), namely, isodense nodule indicating almost the same intranodular arterial blood supply relative to the surrounding liver (type I), hypodense indicating decreased arterial blood supply (type II), a part of the nodule demonstrating hyperdensity indicating a partially increased arterial supply (type III) and entirely hyperdense indicating entirely increased arterial supply (type IV). The correlation between the histologic types of nodules and these CTHA

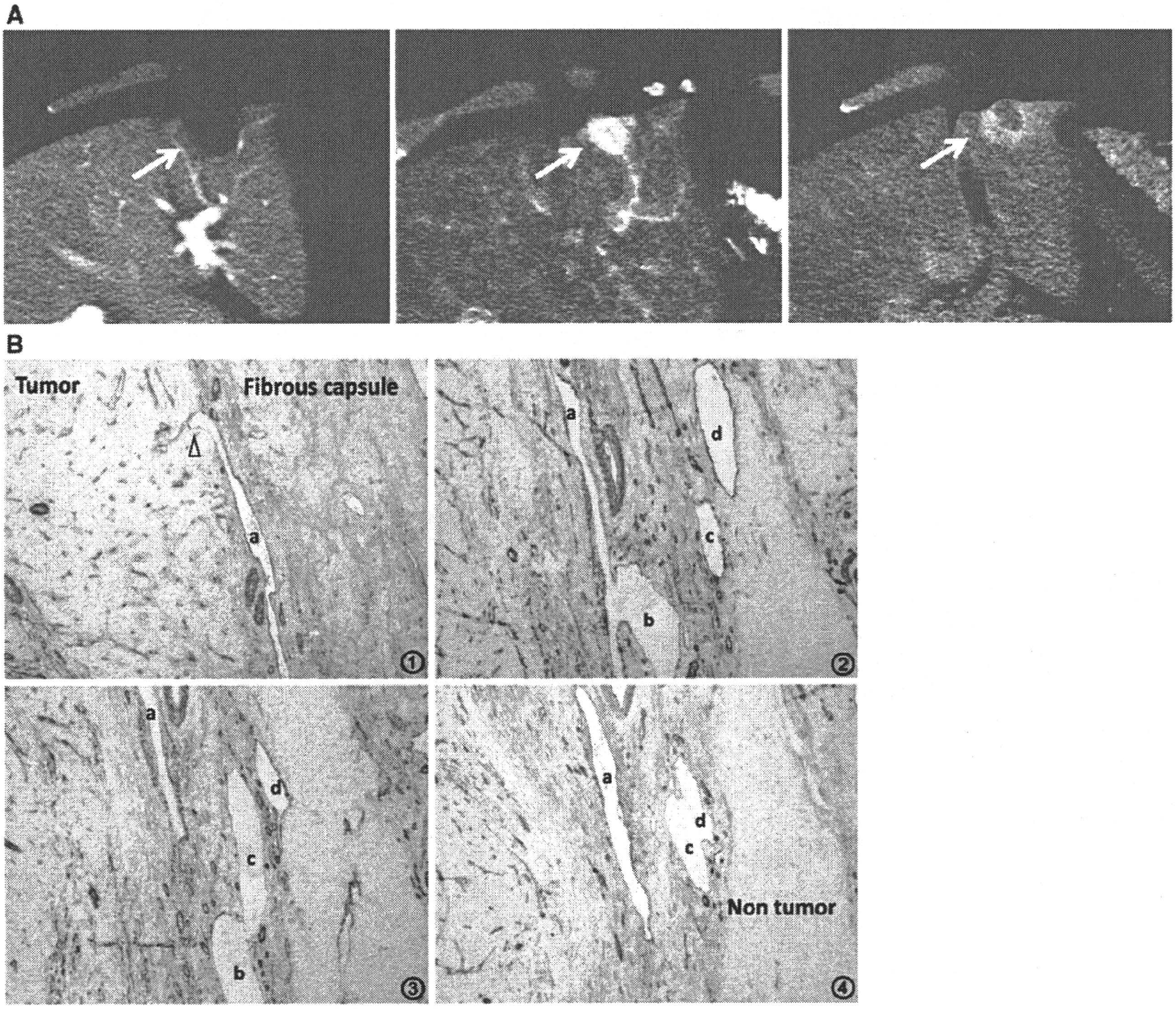

Fig. 7. Moderately differentiated HCC with pseudocapsule formation. **A** CTAP shows an entirely hypodense nodule (*left, arrow*). CTHA demonstrates it as an entirely hyperdense nodule on early phase (*middle, arrow*) with thick corona enhancement on late phase (*right, arrow*). **B** Serial specimens from *1* to *4* with double immunohistochemical staining for CD34 and αSMA show the communication between intracapsular portal venules (*a–d*) and intratumoral blood sinusoids (*arrowheads*) (×100).

findings revealed the significant correlation or strong tendency between type I and L-DN and early HCC, type II and H-DN and early HCC, type III and well-differentiated HCC and type IV and moderately or poorly differentiated HCC (Figs. 3, 4, 5, 6, 7). These results suggested that the intranodular portal supply relative to the surrounding liver parenchyma is decreased, whereas the intranodular arterial supply is first decreased during the early stage of hepatocarcinogenesis and then increased in parallel with increasing grade of malignancy of the nodules as shown in Fig. 8. However, the differences of histological findings among these nodules are sequential, and the exact diagnosis of the entire nodule is occasionally difficult because of internal histological heterogeneity. Therefore, as shown in the original article [7], there was a fairly wide range of overlap in blood supply patterns among the various types of hepatocellular nodules.

To verify the histological background of the findings obtained by CTAP and CTHA, we analyzed morphometrically the vascular supply of DN and HCCs [10, 11], and suggested that the portal tracts including portal vein and hepatic artery were decreased in accordance with increasing grade of malignancy and virtually absent in HCCs. In contrast, abnormal arteries due to tumor angiogenesis developed in H-DN during the course of hepatocarcinogenesis, and were markedly increased in number in moderately differentiated HCCs.

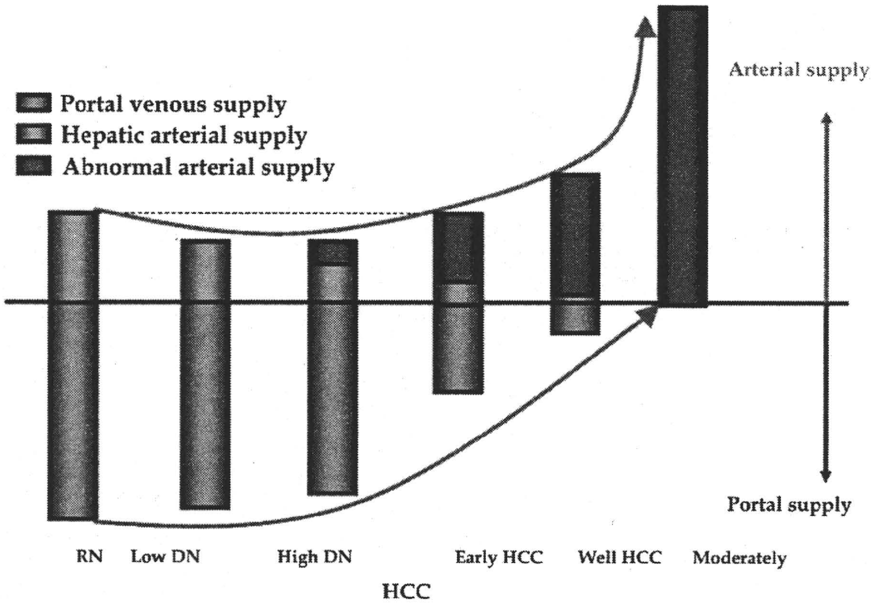

Fig. 8. Multi-step hepatocarcinogenesis and changes of intranodular blood supply. Intranodular portal supply gradually decreases in accordance with the elevation of the grade of malignancy of the nodules and finally disappears in moderately differentiated HCCs. On the other hand, arterial supply first decreases at the early stage of hepatocarcinogenesis and then acutely increases, and finally the entire nodule is fed only by artery in moderately differentiated HCCs.

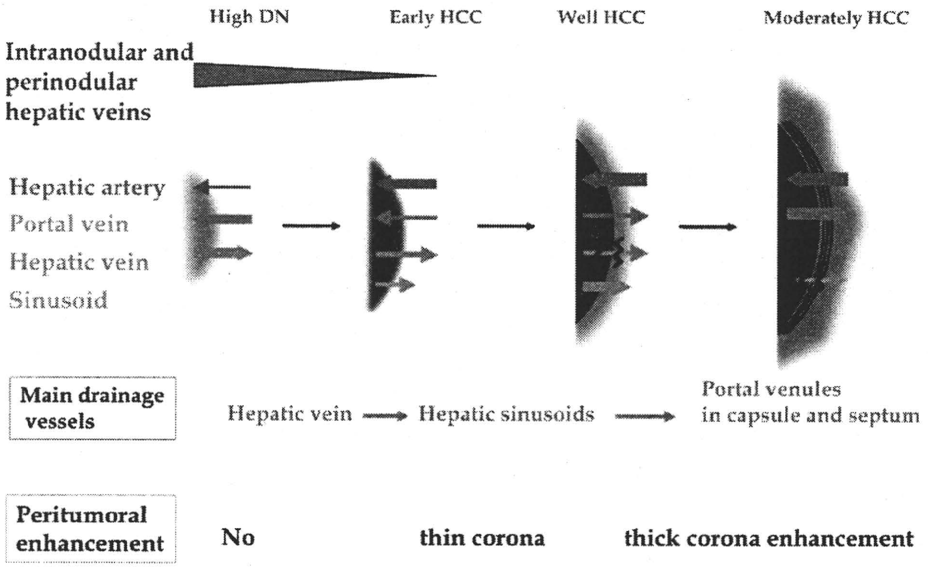

Fig. 9. Multi-step changes of drainage vessels and peritumoral enhancement during hepatocarcinogenesis. In DNs or early HCCs, the main drainage route from the tumor is intranodular or perinodular hepatic vein. However, because hepatic veins disappear from the tumor during very early stage of hepatocarcinogenesis, drainage vessels change to hepatic sinusoids. In moderately differentiated HCC with pseudocapsule formation, the communication between tumor sinusoids and the surrounding hepatic sinusoids are also blocked, and then, the portal venules in the pseudocapsule finally become the main drainage vessel from the tumor. In accordance with the changes of the drainage vessels, thin to thick corona enhancement appears surrounding the tumor.

Multi-step changes of drainage vessels (flow) during hepatocarcinogenesis

By single level dynamic thin-section CT during the bolus injection of a small amount of contrast medium, we revealed in vivo hemodynamics in hypervascular classical HCC, namely, the arterial blood flow into the tumor drains into surrounding hepatic sinusoids (corona enhancement) (Fig. 7) [12]. This drainage was well visualized in the late phase of CTHA which was taken after the stoppage of the infusion of the contrast medium into the hepatic artery. Histological examination revealed continuity between a tumor sinusoid and a portal venule in the pseudocapsule (encapsulated HCC) or surrounding hepatic sinusoids (HCC without pseudocapsule) [11, 12]. According to our recent histological study correlated with CTAP and CTHA, the main drainage vessels of hepatocellular nodules change from hepatic veins to hepatic sinusoids and then to portal veins during multi-step hepatocarcinogenesis, mainly due to disappearance of the hepatic veins from the nodules [11]. Therefore, in early HCC, no perinodular corona enhancement is seen on portal to equilibrium phase CT, but it is definite in hypervascular classical HCC (Figs. 3, 6, 7, 9). Corona enhancement is thicker in encapsulated HCC and thin in HCC without pseudocapsule (Figs. 6, 7, 9). The drainage flow from hypervascular HCC variously modified the imaging findings, a feature useful for differential diagnosis. Drainage from the tumor makes the tumor appear larger than it really is on various kinds of blood flow imaging findings. It is the first site of the intrahepatic metastasis of HCC, and daughter nodules are commonly seen in the drainage area. Iodized oil flowed into the surrounding liver through this drainage route and enhanced the effect of transcatheter arterial chemoembolization [13]. The drainage area should be included in RFA area to prevent local recurrence.

Hemodynamics of other hepatic cancers

Metastatic liver cancers show thin corona enhancement or early peritumoral enhancement on single-level dynamic CTHA [14]. We named the former as "drainage pattern" and the latter as "arterio-portal (AP) shunt pattern". In cases with drainage pattern, the tumor shows hypervascularity in early phase and thin peritumoral enhancement in late phase similar to hypervascular HCC without pseudocapsule, and the drainage route may be the connection between tumor sinusoids and hepatic sinusoids surrounding the tumor [14, 15]. In cases with AP shunt pattern, the tumor shows no definite enhancement except faint staining on the peripheral margin of the tumor, but early peritumoral enhancement with occasional wedge-shaped expansion is seen. The mechanism of this early enhancement is unknown, but peritumoral multicentric AP shunts due to the obstruction of the portal or hepatic venules can be one of the possible causes. Because abundant fibrous tissue is often contained in this kind of tumor, internal delayed enhancement is commonly associated. Mass-forming type of cholangiocarcinoma usually demonstrates AP shunt pattern. Among malignant primary liver cancer, cholangiolocellular carcinoma (bile ductular carcinoma) shows unique hemodynamics [16]. It typically shows tumor hypervascularity with surrounding enhancement resembling AP shunt pattern in early phase and delayed internal enhancement on late phase, probably due to abundant cancer cells and fibrous tissues in the tumor with multiple entrapped portal tracts in the tumor (replacing infiltration type growth with the portal tracts incorporated into the tumor). Benign hypervascular hepatic masses such as cavernous hemanigoma, focal nodular hyperplasia (FNH) [17], angiomyolipoma and peliosis hepatis usually do not show corona enhancement, probably due to main drainage to hepatic vein. Two exceptions are hepatic adenoma and hypervascular hyperplastic nodule associated with alcoholic cirrhotic livers which commonly demonstrate corona enhancement [18]. Understanding these hemodynamic differences among various kinds of hepatic mass lesions are important for differential diagnosis and treatment.

In conclusion, it is very important to know the hemodynamics of HCCs and related hepatocellular nodules for the understanding of pathophysiology and precise imaging diagnosis and treatment of HCCs. For this purpose, angiography-assisted CT is most valuable and accurate, but because of its invasiveness, blood flow imaging with contrast ultrasound, dynamic CT and MR imaging is necessary.

References

1. Ikai I, Arii S, Okazaki M, et al. (2007) Report of the 17th nationwide follow-up survey of primary liver cancer in Japan. Hepatol Res 37:676–691
2. Matsui O, Kadoya M, Suzuki M, et al. (1983) Work in progress: dynamic sequential computed tomography during arterial portography in the detection of hepatic neoplasms. Radiology 146:721–727
3. Matsui O, Takashima T, Kadoya M, et al. (1985) Dynamic computed tomography during arterial portography: the most sensitive examination for small hepatocellular carcinomas. J Comput Assist Tomogr 9:19–24
4. Hayashi M, Matsui O, Ueda K, et al. (1999) Correlation between the blood supply and grade of malignancy of hepatocellular nodules associated with liver cirrhosis: evaluation by CT during intraarterial injection of contrast medium. AJR Am J Roentgenol 172:969–976
5. International Consensus Group for Hepatocellular Neoplasia (2009) Pathologic diagnosis of early hepatocellular carcinoma: a report of the international consensus group for hepatocellular neoplasia. Hepatology 49:658–664
6. Ferrara N (2004) Vascular endothelial growth factor: basic science and clinical progress. Endocr Rev 25:581–611
7. Nakamura K, Zen Y, Sato Y, et al. (2007) Vascular endothelial growth factor, its receptor Flk-1, and hypoxia inducible factor-1alpha are involved in malignant transformation in dysplastic nodules of the liver. Hum Pathol 38:1532–1546
8. Park YN, Kim YB, Yang KM, et al. (2000) Increased expression of vascular endothelial growth factor and angiogenesis in the early stage of multistep hepatocarcinogenesis. Arch Pathol Lab Med 124:1061–1065
9. Matsui O, Kadoya M, Kameyama T, et al. (1991) Benign and malignant nodules in cirrhotic livers: distinction based on blood supply. Radiology 178:493–497
10. Ueda K, Terada T, Nakanuma Y, Matsui O (1992) Vascular supply in adenomatous hyperplasia of the liver and hepatocellular carcinoma: a morphometric study. Hum Pathol 23:619–626

11. Kitao A, Zen Y, Matsui O, Gabata T, Nakanuma Y (2009) Hepatocarcinogenesis: multistep changes of drainage vessels at CT during arterial portography and hepatic arteriography–radiologic-pathologic correlation. Radiology 252:605–614
12. Ueda K, Matsui O, Kawamori Y, et al. (1998) Hypervascular hepatocellular carcinoma: evaluation of hemodynamics with dynamic CT during hepatic arteriography. Radiology 206:161–166
13. Terayama N, Matsui O, Gabata T, et al. (2001) Accumulation of iodized oil within the nonneoplastic liver adjacent to hepatocellular carcinoma via the drainage routes of the tumor after transcatheter arterial embolization. Cardiovasc Intervent Radiol 24:383–387
14. Terayama N, Matsui O, Ueda K, et al. (2002) Peritumoral rim enhancement of liver metastasis: hemodynamics observed on single-level dynamic CT during hepatic arteriography and histopathologic correlation. J Comput Assist Tomogr 26:975–980
15. Liu Y, Matsui O (2007) Changes of intratumoral microvessels and blood perfusion during establishment of hepatic metastases in mice. Radiology 243:386–395
16. Kozaka K, Matsui O, Nakanuma Y, et al. (2007) A subgroup of intrahepatic cholangiocarcinoma with an infiltrating replacement growth pattern and a resemblance to reactive proliferating bile ductules: 'bile ductular carcinoma'. Histopathology 51:390–400
17. Miyayama S, Matsui O, Ueda K, et al. (2000) Hemodynamics of small hepatic focal nodular hyperplasia: evaluation with single-level dynamic CT during hepatic arteriography. AJR Am J Roentgenol 174:1567–1569
18. Kobayashi S, Matsui O, Kamura T, et al. (2007) Imaging of benign hypervascular hepatocellular nodules in alcoholic liver cirrhosis: differentiation from hypervascular hepatocellular carcinoma. J Comput Assist Tomogr 31:557–563

Radiol Phys Technol
DOI 10.1007/s12194-010-0110-1

Effectiveness of temporal and dynamic subtraction images of the liver for detection of small HCC on abdominal CT images: comparison of 3D nonlinear image-warping and 3D global-matching techniques

**Eiichiro Okumura · Shigeru Sanada ·
Masayuki Suzuki · Akihiro Takemura ·
Osamu Matsui**

Received: 28 July 2010 / Revised: 4 December 2010 / Accepted: 6 December 2010

Abstract Misregistration errors occur at the periphery of the hepatic region due to respiratory- and interval-related changes in hepatic shape. To reduce these misregistration errors, we developed a temporal and dynamic subtraction technique to enhance small hepatocellular carcinoma (HCC) by using a 3D nonlinear image-warping technique. The study population consisted of 21 patients with HCC. We registered the present and previous arterial-phase CT images or the present nonenhanced and arterial-phase CT images obtained in the same position by 3D global-matching plus 3D nonlinear image-warping. Temporal subtraction images were obtained by subtraction of the previous arterial-phase CT image from the warped present arterial-phase CT image. Dynamic subtraction images were obtained by subtraction of the present nonenhanced CT image from the warped present arterial-phase CT image. When we used this new technique, the number of good or excellent cases increased from 14.2% (3/21 cases) to 71.4% (15/21 cases) on temporal subtraction images. With this technique, subjective rating scores for image quality improved in 57.1% of cases (12/21 cases) on temporal subtraction images and 81.0% of cases (17/21 cases) on dynamic subtraction images. The results indicated that the new subtraction images were greatly improved by use of the 3D nonlinear image-warping technique.

E. Okumura (✉)
Department of Medical Radiological Technology,
Kagoshima Medical Technology College,
5417-1 Hirakawa, Kagoshima 891-0133, Japan
e-mail: rt.okumura@harada-gakuen.ac.jp

S. Sanada · M. Suzuki · A. Takemura · O. Matsui
Department of Radiological Technology,
Graduate School of Medical Sciences, Kanazawa University,
5-11-80 Kodatsuno, Kanazawa 920-0942, Japan

Keywords Computer-aided diagnosis (CAD) · Nonlinear volume image warping · Computed tomography (CT) · Hepatocellular carcinoma (HCC) · Temporal and dynamic subtraction technique

1 Introduction

Hepatocellular carcinoma (HCC) occurs in patients with chronic liver disease and cirrhosis, providing an identifiable risk group of patients for screening [1]. HCC accounts for 6% of all human cancers worldwide, being the fifth and the tenth most common malignancy in men and women, respectively [2, 3]. Therefore, contrast-enhanced helical computed tomography (CT) examinations have been used as a screening tool for detecting HCC in patients with cirrhosis [1]. Hypervascular moderately differentiated HCC usually exhibits early enhancement on arterial-phase CT images and ring enhancement on delayed-phase CT images [4]. However, false-positive results were reported in cases of small arterial-portal venous shunt (A-P shunt) that were misinterpreted as HCC because of their nodular appearance and unequivocal arterial-phase enhancement on multi-detector CT [1]. That study confirmed that a substantial false-positive diagnosis rate (8%) of HCC occurs in an experienced liver transplantation center, with 5% of the lesions appearing hypoattenuated relative to the liver and 3% showing substantial enhancement on arterial-phase CT images [5, 6]. Therefore, the sensitivity of HCC in cirrhotic livers prior to transplantation ranged from 33 to 71% in spatial and temporal resolution on multi-detector CT [7]. The prospective and retrospective sensitivities of triphasic helical CT for detecting HCC were 59–68% [5]. It is especially difficult for radiologists to distinguish true HCC from a small nodular A-P shunt in patients with hepatic cirrhosis. To assist radiologists in follow-up examination, we have developed a computer-aided detection (CAD) system for detecting increases in the size of nodular early enhancement and new enhancement on temporal and dynamic subtraction with a 3D global-matching technique plus a 2D nonlinear image-warping technique (previous technique) [8, 9].

Cases with suspected A-P shunt that increases in size over time have an increased likelihood of moderately differentiated HCC, and temporal subtraction images show ring enhancement in such cases [8].

However, because misregistration errors in these cases were caused by a 3D deformity that involved craniocaudal, lateral, and anterior-posterior deformation, most hepatic regions were not well registered, and misregistration artifacts appeared throughout the whole and/or half of the periphery of hepatic regions in two cases. Therefore, it was difficult to select images from the same anatomic positions as with the previous technique in such cases.

In recent years, many automated methods for the registration of images have been developed [10–18]. Registration techniques reported to date used tomographic modalities, such as CT, magnetic resonance (MR) imaging, single-photon emission computed tomography (SPECT), and positron emission tomography (PET) at the same position of the hepatic [10–13] and lung regions [14, 15]. Point- and voxel-based registrations were used for similarity measurements on registration between two CT images [16]. The voxel-based methods employ image intensity information with mathematical similarity measures such as the sum of the squared distance (SSD), correlation coefficient (CC), correlation ratio (CR), or mutual information (MI), or iterative determination of deformations based on image gradients such as the optical-flow method [17, 18].

In this study, for further reduction of these misregistration errors in temporal and dynamic subtraction images [9], a 3D nonlinear image-warping technique was employed for accurate registration of local deformation patterns included in two images for detection of small HCC.

2 Materials and methods

2.1 Materials

Twenty-one pairs of upper abdominal CT images with HCC (15 men and 6 women; mean age 66.3 years) were included. Each patient underwent nonenhanced and arterial-phase CT imaging which use of a Hispeed Nx/I scanner (120 kVp and 200 mA; GE Yokogawa Medical Systems, Tokyo, Japan) at 512 × 512 pixels with a slice thickness of 1.25–3.75 mm. The previous and present images were obtained from October 2002 to June 2004, and the mean interval between images was 208 ± 109 days (range 84–493 days).

2.2 Improved temporal and dynamic subtraction technique scheme

The overall scheme of the temporal subtraction technique is illustrated in Fig. 1. We detected the hepatic region on the present and previous arterial-phase CT images. With a 3D global-matching technique with use of volumetric CT images, we registered the present and previous arterial-phase CT images obtained in roughly the same position of the hepatic region. Next, the present arterial-phase CT images were accurately registered with the previous arterial-phase CT images by use of a new 3D nonlinear image-warping technique for reducing the misregistration error at the movable and deformable periphery of the hepatic regions. Finally, the warped present arterial-phase CT images were subtracted from previous arterial-phase CT

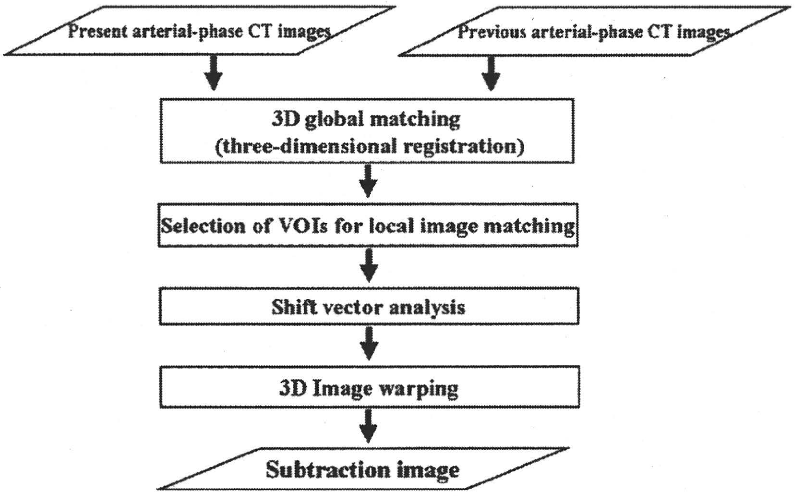

Fig. 1 Overall scheme of the improved temporal subtraction technique

images to provide new temporal subtraction images. In addition, we registered the present arterial-phase and nonenhanced CT images at the same position in the same manner as described above. The warped present arterial-phase CT images were subtracted from the present nonenhanced CT images to provide dynamic subtraction images.

2.3 3D detection of the hepatic regions

The present nonenhanced arterial-phase CT images and the previous arterial-phase CT images were smoothed. A quadrilateral region of interest (ROI) was set manually at the center of the hepatic region on the reference image, which was in the middle in the craniocaudal position of the hepatic region. We determined the threshold value of the hepatic region in this ROI by histogram analysis with the mode method and binarized all images by using this threshold value. On the present and previous arterial-phase CT images, we employed a twice erosion processing (3 × 3 × 3 pixels) to eliminate the extrahepatic region. The labeled regions of the maximum volume were detected as the hepatic regions. We employed twice dilation processing (3 × 3 × 3 pixels) to fill the intrahepatic region. However, by comparison with the present and previous arterial-phase CT images, it was often difficult to extract all hepatic regions on the present nonenhanced CT images because the CT numbers of the hepatic regions were similar to those of the spleen and other organs surrounding the hepatic region. Therefore, on the present nonenhanced CT images, we employed a third erosion processing (3 × 3 × 3 pixels) to eliminate the extrahepatic region. The labeled regions of the maximum volume were detected as the hepatic regions. We employed a third dilation processing (3 × 3 × 3 pixels) to fill the intrahepatic region.

2.4 3D global-matching technique

Rigid body registration was generally sufficient for intramodality registration application for organs that do not change significantly in shape, such as the brain [12]. Most rigid registration techniques were processed by iterative adjustment of the transformation and rotation to maximize some similarity measure (SSD, CC, and CR, etc.) between a transformed and rotated template image and a corresponding reference image [19]. Therefore, in this study, we globally matched the hepatic region of volume data on abdominal CT images with this rigid registration (3D global-matching technique) [9].

The overall scheme of the 3D global-matching technique is illustrated in Fig. 2. The registration technique was based on geometric transformations, which are mappings of points from "space *X*" of one volume data set to "space *Y*" of another volume data set. First, we set binarized the present arterial-phase CT images of volume data as template images (space *X*) and set binarized the previous arterial-phase CT image of volume data as reference images (space *Y*). The rigid transformation was limited to translation and rotation. The rigid transformation was also a simple class with only six parameters completely specifying the rigid transformation in

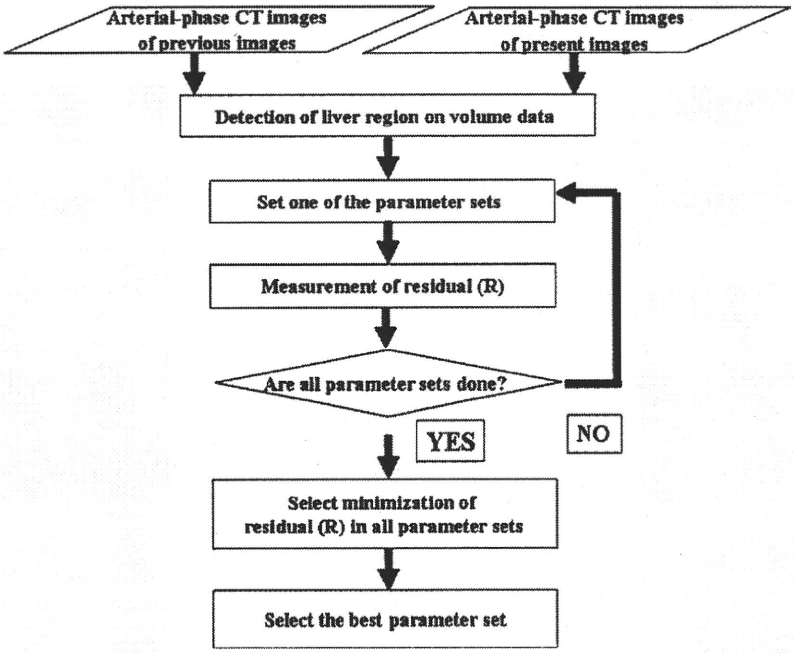

Fig. 2 3D global-matching technique

three dimensions. We determined the T orthogonal matrix with transformation and rotation by using the following equation:

$$X = TY$$

$$T = \begin{pmatrix} 1 & 0 & 0 & \text{center}X + \text{shift}X \\ 0 & 1 & 0 & \text{center}Y + \text{shift}tY \\ 0 & 0 & 1 & \text{center}Z + \text{shift}tZ \\ 0 & 0 & 0 & 1 \end{pmatrix} \begin{pmatrix} 1 & 0 & 0 & 0 \\ 0 & \cos\theta_x & -\sin\theta_x & 0 \\ 0 & \sin\theta_x & \cos\theta_x & 0 \\ 0 & 0 & 0 & 1 \end{pmatrix}$$
$$\begin{pmatrix} \cos\theta_y & 0 & \sin\theta_y & 0 \\ 0 & 1 & 0 & 0 \\ -\sin\theta_y & 0 & \cos\theta_y & 0 \\ 0 & 0 & 0 & 1 \end{pmatrix}$$
$$\begin{pmatrix} \cos\theta_z & -\sin\theta_z & 0 & 0 \\ \sin\theta_z & \cos\theta_z & 0 & 0 \\ 0 & 0 & 1 & 0 \\ 0 & 0 & 0 & 1 \end{pmatrix} \begin{pmatrix} 1 & 0 & 0 & -\text{center}X \\ 0 & 1 & 0 & -\text{center}Y \\ 0 & 0 & 1 & -\text{center}Z \\ 0 & 0 & 0 & 1 \end{pmatrix},$$

where T was a 4 × 4 orthogonal matrix and included the transformation and rotation. Six parameters—i.e., translation along the x-axis (shift X), y-axis (shift Y), and z-axis (shift Z), and the rotation angle around the x-axis (θ_x), y-axis (θ_y), and z-axis (θ_z) on volume data—were used in the rigid registration technique. Space X was specified by three coordinates (x, y, z) on the present arterial-phase CT image of volume data. Space Y was specified such that coordinates (x', y', z') were transformed and rotated in space X. The parameters of the transformation shift along each axis were configured into a distance of ±13.7 mm from the center coordinates (center X, center Y, center Z) of the template image, whereas the parameters of the rotation angle were configured to ±10° from the center coordinates of the template image [9].

To examine the resemblance of volume data on the hepatic region between the present (A) and previous (B) arterial-phase CT images, we determined the residual, R, by the following equation:

$$R = \sum_{i=1}^{L}\sum_{j=1}^{M}\sum_{k=1}^{N} |A(i,j,k) - B(i,j,k)|,$$

where L, M, and N indicate the voxel sizes of the area selected for the volume data. If the volume data in the two images are identical, R will be calculated as having a minimum value of 0.

After completion of one of the six parameter sets, the residual was measured by use of this parameter set. After completion of the procedure for all parameter sets, the most appropriate parameter set that produced the least residual in the matching procedure was selected by the registration technique (Fig. 2).

In addition, we produced the binarized present arterial-phase CT images as the template images and the binarized nonenhanced CT images as the reference images. We then registered the present arterial-phase CT images and nonenhanced CT images at the same position according to the procedure described above [9].

2.5 Temporal and dynamic subtraction technique with 3D nonlinear image-warping technique

First, we employed a global transformation, i.e., rotation and translation, on the hepatic region with the 3D global-matching technique. However, 3D deformation and movement of the hepatic region during CT examinations gave the greatest registration error on the temporal and dynamic subtraction images with this technique [9]. A nonlinear image-warping technique has been used successfully in temporal subtraction and contralateral subtraction applied to chest radiographs and chest CT images [20–26]. Therefore, in the new scheme, we employed a 3D nonlinear image-warping technique to improve the local deformation of the hepatic region.

Template volumes of interest (VOIs) and the corresponding search area VOIs were automatically located on the present and previous arterial-phase CT images (Fig. 3). It is important to note that the background area was excluded

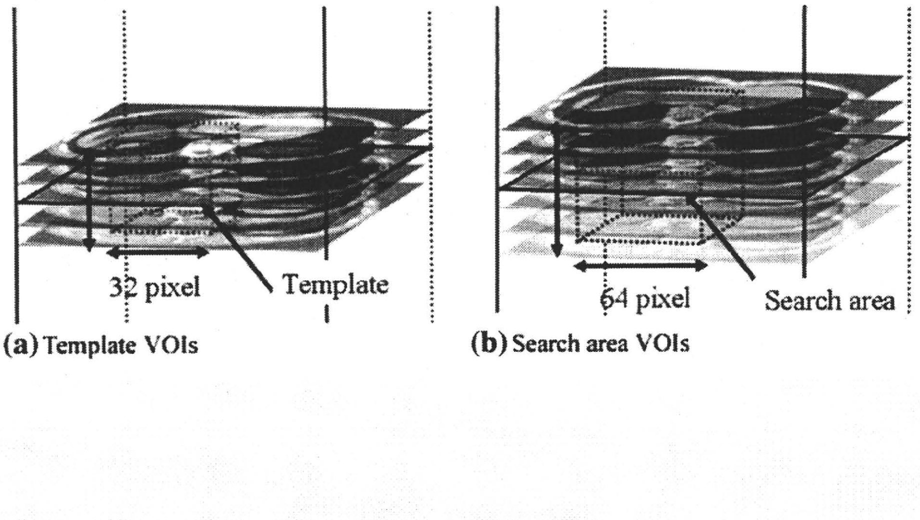

(a) Template VOIs **(b)** Search area VOIs

Fig. 3 3D nonlinear image warping technique

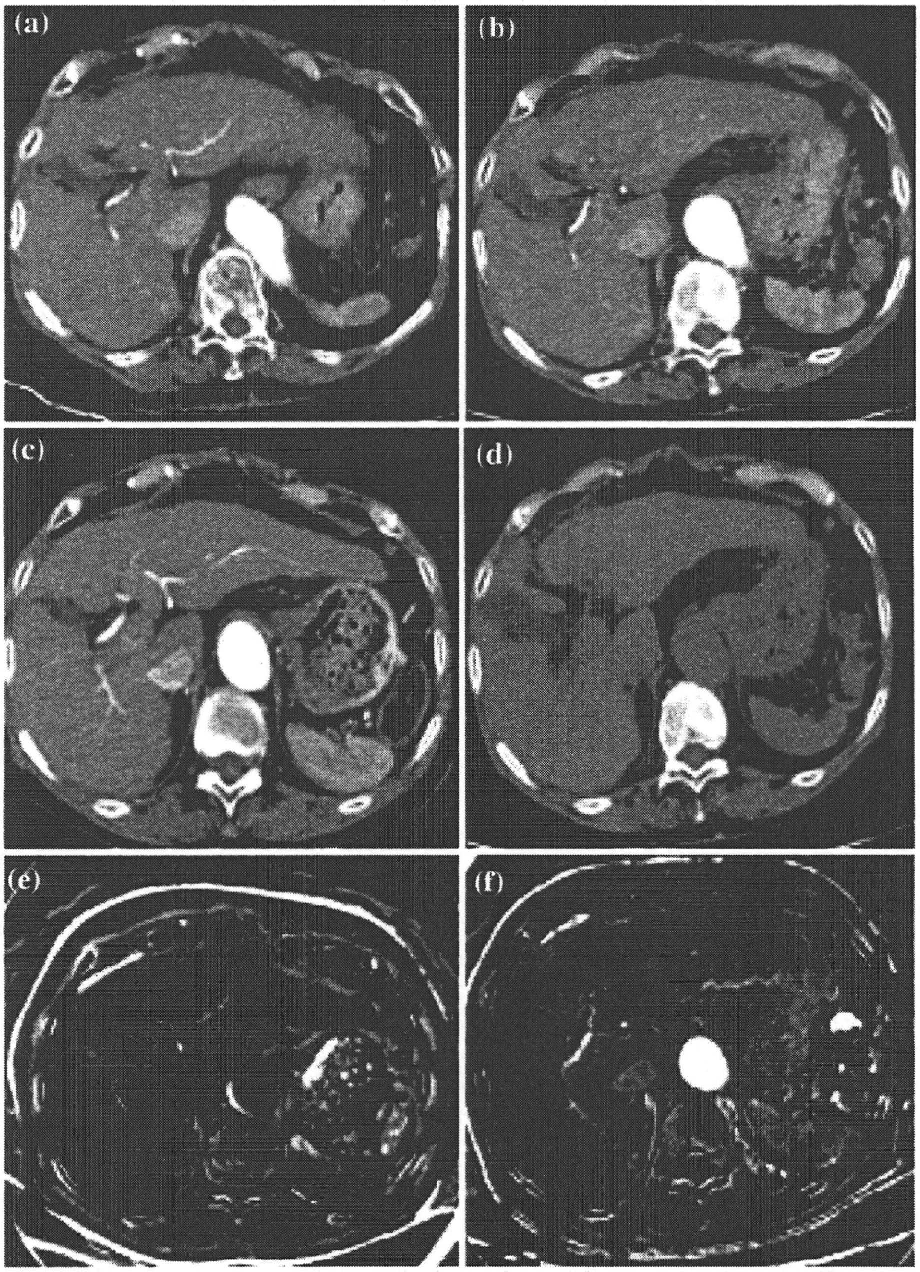

Fig. 4 Temporal and dynamic subtraction images obtained by use of the new technique. **a**, **b** Arterial-phase CT images. **c** Previous arterial-phase CT image. **d** Present nonenhanced CT image. **e** Temporal subtraction image (**a**–**c**) and **f** dynamic subtraction images (**b**–**d**)

from the selection of VOIs because these regions do not contain useful information for image matching. The matrix sizes of the template and search area VOIs were 32 × 32 × 32 and 64 × 64 × 64 pixels, respectively. The distance between the adjacent VOIs was 16 pixels. A cross-correlation technique was used for determining the similarities between the template VOIs and the search area VOIs [25, 26]. Once the template VOIs and search area VOIs were determined, the cross-correlation technique was used for performing local image matching for determination of the shift vectors (Δx, Δy, Δz) in orthogonal directions [25, 26]. These shift vectors indicated a shift in the coordinates on the center of the search area VOI, and they provided the best matched of the template VOIs with the corresponding "matched" area in the search area VOIs. The shift vectors with the maximum correlation value were not necessarily the "correct" shift vectors. Therefore, in this study, the shift vectors were smoothed (kernel size: 32 × 32 × 32 pixel) to reduce misregistration errors, and 3D surface fitting by use of a B-spline curve [10, 27] was applied to Δx, Δy, and Δz of the mapped shift vectors. This B-spline curve method placed a uniformly spaced 3D grid over the hepatic volume data.

Table 1 Distribution of the number of cases with different subjective rating scores for the quality of temporal (*A*) and dynamic (*B*) subtraction images obtained with the standard and new technique

	1 (very poor)	2	3 (fair)	4	5 (excellent)
(*A*)					
3D registration		2 (9.5%)	16 (76.2%)	3 (14.2%)	
3D registration plus 3D image warping		2 (9.5%)	4 (19.0%)	15 (71.4%)	
(*B*)					
3D registration		1 (4.8%)	11 (52.4%)	9 (42.9%)	
3D registration plus 3D image warping		1 (4.8%)	2 (9.5)	17 (81.0%)	1 (4.8%)

Table 2 Distribution of the number of cases affected by the new technique in terms of subjective rating score on the quality of subtraction images

	−2 (definitely degraded)	−1	0 (no charge)	+1	+2 (clearly improved)
(*A*)					
3D registration plus 3D image warping		1 (4.8%)	8 (38.1%)	12 (57.1%)	
(*B*)					
3D registration plus 3D image warping			4 (19.0%)	17 (81.0%)	

Temporal (*A*) and dynamic (*B*) subtraction images with the new technique in comparison with those obtained with the standard technique

Displacement of each shift vector resulted in deformation of the region surrounding the points in a way that made the overall deformation as smooth as possible [27]. The displacement was easily calculated by use of cubic polynomials. We used a lattice with 3 × 3 × 3 control points (32 × 32 × 32 pixels). This allowed for 27 × 15 degrees of freedom in the determination of B-spline registration.

In addition, the template VOIs and the corresponding search area VOIs were automatically located on the present arterial-phase and nonenhanced CT images. We then performed 3D surface fitting by using the B-spline curve in the same manner as described above.

Figure 4a–f shows the temporal subtraction image and dynamic subtraction image with the 3D global-matching technique plus the 3D nonlinear image-warping technique (new technique), respectively. The temporal subtraction image was obtained by subtraction of the previous arterial-phase CT image from the warped present arterial-phase CT images obtained in the same position of the hepatic regions by use of the new technique. The dynamic subtraction image was obtained by subtraction of the present nonenhanced CT image from the warped present arterial-phase CT image obtained at the same position of the hepatic regions by use of the new technique; this took a central processing unit (CPU) time of approximately 2 h on a personal computer with a 2.0-GHz CPU.

2.6 Subjective evaluation of quality of temporal and dynamic subtraction images

We evaluated misregistration artifacts on both subtraction images with the new technique and with the 3D global-matching technique alone (standard technique). Briefly, the quality of both subtraction images was evaluated subjectively based on consensus by an experienced radiologist, a medical physicist, and three radiologic technologists. A five-point rating score was used in this study [9, 21–23]:

(a) 5 (excellent): All hepatic regions were perfectly registered.
(b) 4 (good): Most hepatic regions were almost completely registered, with very minor misregistration errors.
(c) 3 (fair): Most hepatic regions were well registered, with some minor misregistration.
(d) 2 (poor): Most hepatic regions were not well registered, and misregistration errors were observed.
(e) 1 (very poor): Most hepatic regions were registered and appeared in the entire periphery of the hepatic regions.

Another rating method was also used for examination of the changes in the quality of both subtraction images obtained with the previous and the new technique [9, 21–23]. The rating score ranged from −2 to +2, as listed below. The quality of the subtraction images was:

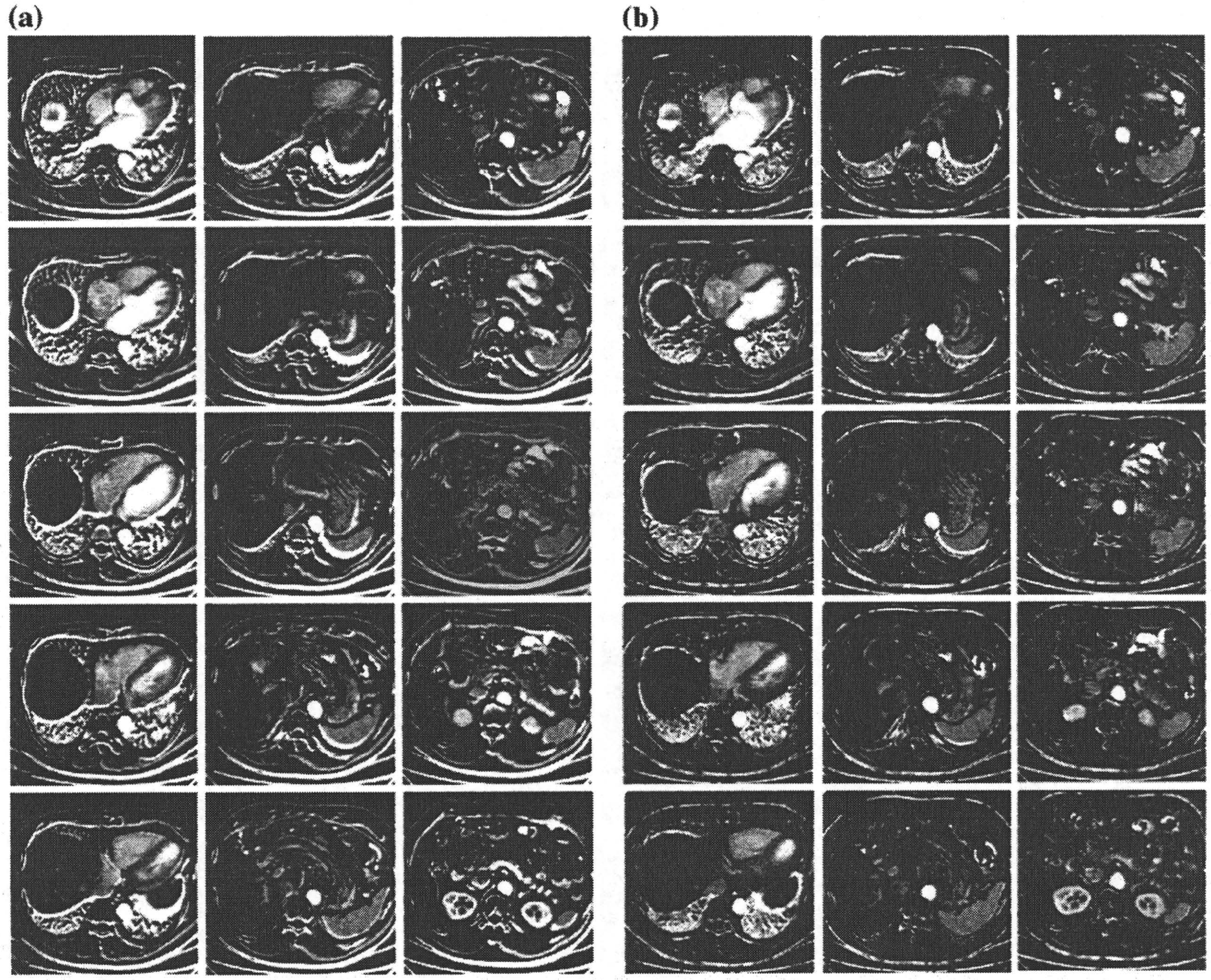

Fig. 5 Comparison of **a** dynamic subtraction images with the standard technique with the greatest misregistration error and **b** improved dynamic subtraction images obtained with the new technique

(a) +2 (markedly improved),
(b) +1 (moderately improved),
(c) 0 (unchanged),
(d) −1 (moderately degraded), and
(e) −2 (markedly degraded).

If the majority of the observers (at least three observers) reached the same rating score, this score was adopted. If the five observers provided five different rating scores, the median score was used.

3 Results

Table 1 shows the numbers of cases receiving different subjective rating scores for the quality of the temporal and dynamic subtraction images obtained with the standard technique and the new technique, respectively. With the new technique, the number of good or excellent cases increased from 14.2% (3/21 cases) to 71.4% (15/21 cases) on temporal subtraction images (Table 1A). With this new technique, the number of good or excellent cases increased from 42.9% (9/21 cases) to 85.7% (18/21 cases) on dynamic subtraction images (Table 1B). Table 2 shows the changes in the subjective rating score for the quality of the temporal (Table 2A) and dynamic (Table 2B) subtraction images obtained with the standard technique and the new technique, respectively. With this new technique, subjective rating scores for image quality improved in 57.1% (12/21 cases) on temporal subtraction images and 81.0% (17/21 cases) on dynamic subtraction images (Table 2). Figure 5a, b shows the dynamic subtraction images obtained with the standard technique and the new technique, respectively. With use of the new technique, the misregistration error in the global hepatic region on

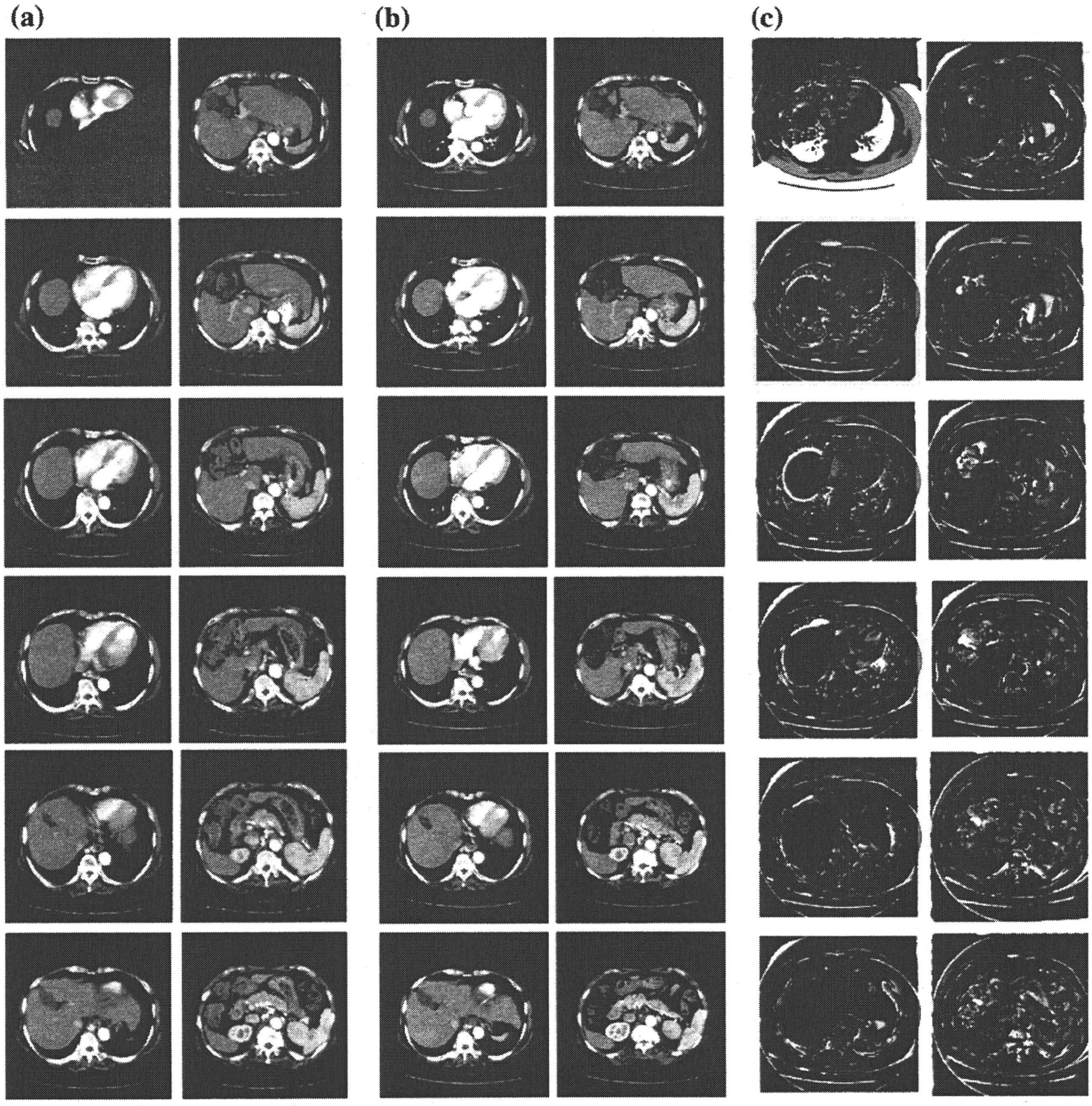

Fig. 6 Very minor misregistration errors on temporal subtraction images with the new technique. Temporal subtraction images (**c**) were obtained by subtraction of the previous arterial-phase CT images (**b**) from the warped present arterial-phase CT images (**a**) obtained at the same position of the liver

dynamic subtraction images was reduced. Specifically, the image quality showed perfect registration on the lower hepatic regions.

Figure 6c shows very minor misregistration errors on the temporal subtraction images with this new technique. The previous arterial-phase CT images (Fig. 6b) and the warped present arterial-phase CT images (Fig. 6a) were automatically selected images set at the same anatomic positions by this new technique. These temporal subtraction images showed very minor misregistration errors. Specifically, the lower hepatic regions were perfectly registered between present and previous arterial-phase CT images. However, these temporal subtraction images on the hepatic region ($S_{2/3}$) showed a misregistration error that deformed

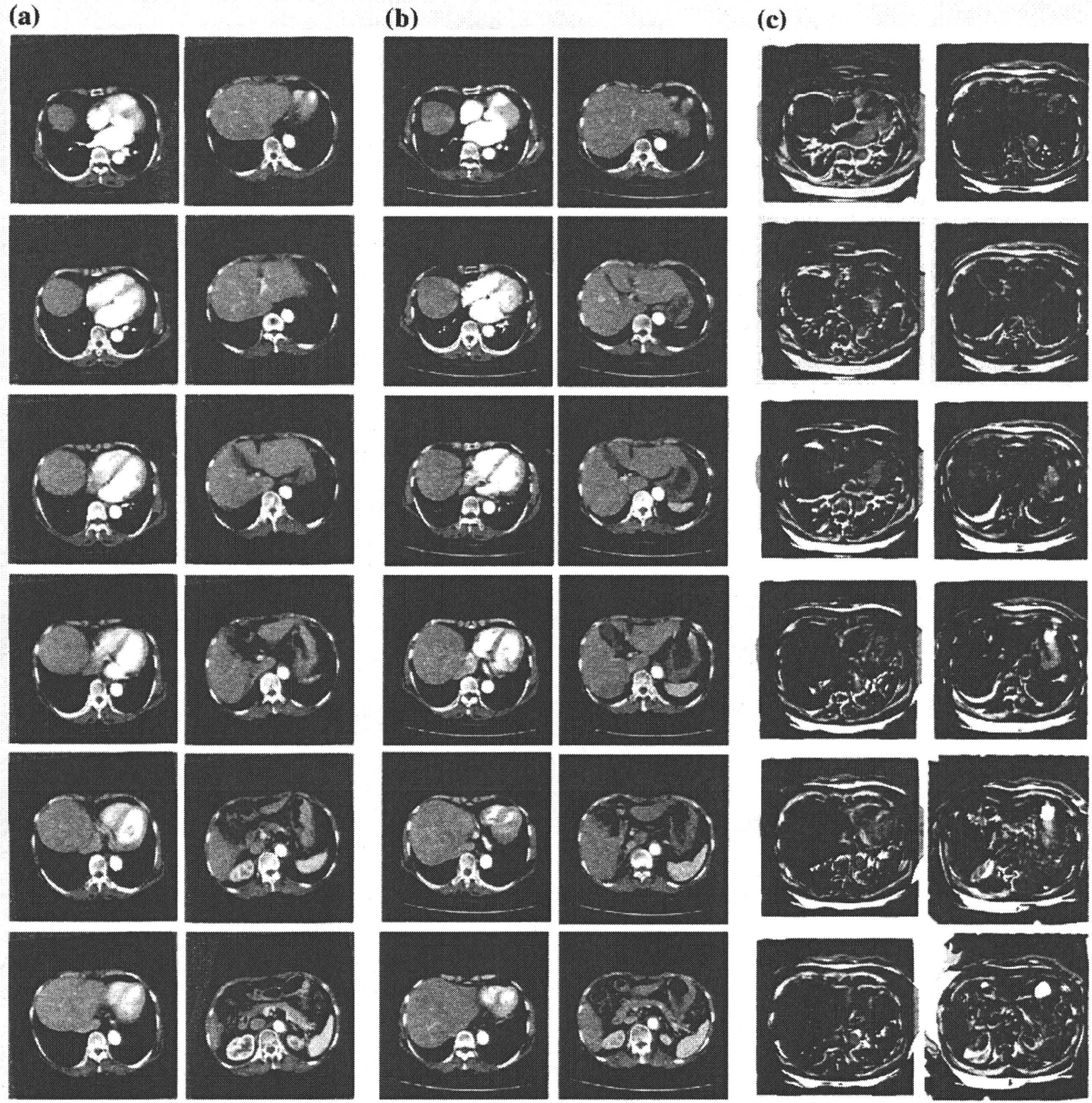

Fig. 7 Misregistration errors on temporal subtraction images with the new technique. Temporal subtraction images (**c**) were obtained by subtraction of the previous arterial-phase CT images (**b**) from the warped present arterial-phase CT images (**a**) obtained at the same position of the liver. Most hepatic regions were not well registered between the present and previous arterial-phase CT images. Temporal subtraction images showed misregistration error

the local hepatic region. Figure 7c shows a very poor misregistration error on the temporal subtraction images with the new technique. The same anatomic positions of the present arterial-phase CT images (Fig. 7a) were very different from those of the previous arterial-phase CT images (Fig. 7b) for the 3D hepatic movement and deformation during a single breath-hold. Therefore, most hepatic regions were not well registered, and misregistration errors occurred.

4 Discussion

In the previous scheme, with the 3D global-matching technique, 3D hepatic regions were matched on images of the same anatomic positions between two sets of volume data. In addition, the 2D nonlinear image-warping technique was used on each axial image for local deformation of the hepatic region [9]. However, many recent studies

Fig. 8 Comparison of **a** temporal subtraction images with the previous technique with the greatest misregistration error and **b** improved temporal subtraction images obtained with the new technique

(a) The temporal subtraction image with the new technique

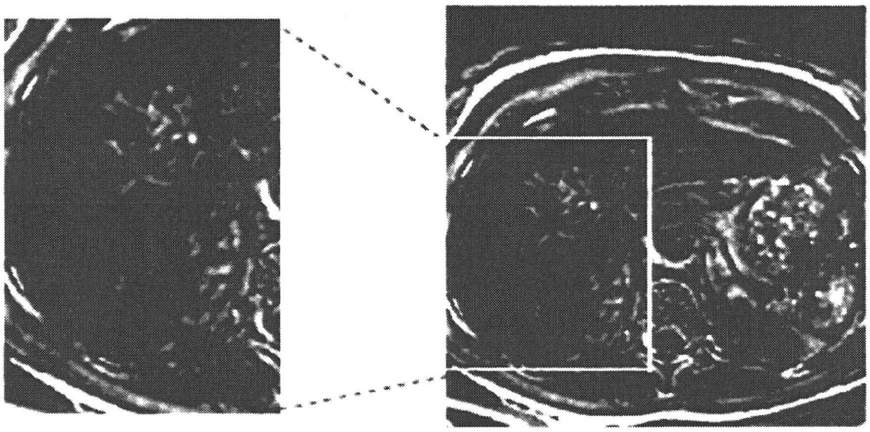

(b) The temporal subtraction image with the previous technique

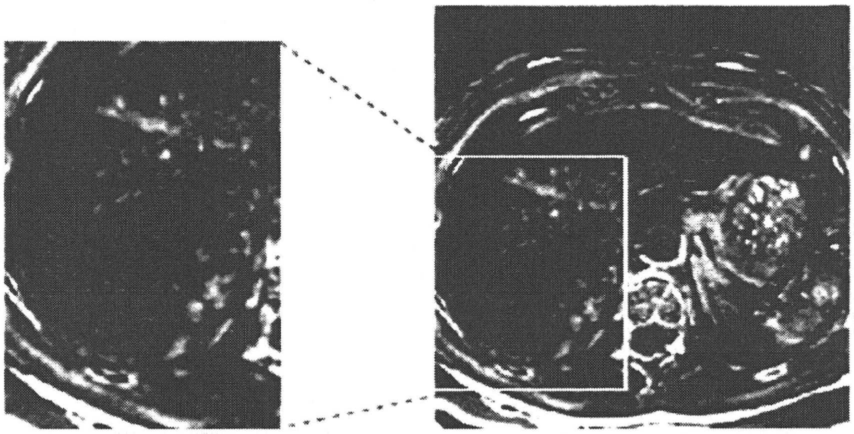

indicated 3D movement and deformation on global and/or local hepatic regions during breath-holding [10, 28–31]. Figure 8a, b shows the temporal subtraction images obtained with the previous technique and the new technique. The temporal subtraction images with the previous technique show misregistration errors at the periphery of the liver and intrahepatic vascular structures, and these images with the new technique showed moderate improvement of these misregistration errors. Nguyen et al. [28] reported that population motion provides a biomechanical reference template for the average liver motions, which were found to be 0.12 ± 0.10, 0.84 ± 0.13, and 1.24 ± 0.18 cm in the left–right (LR), anterior–posterior (AP), and superior–inferior (SI) directions, respectively. We developed temporal and dynamic subtraction with this new technique to reduce the misregistration error in the local deformation of the hepatic region. Therefore, the 3D nonlinear image-warping technique indicated a better performance for registration of the same anatomic position of the hepatic region than did the 3D global-matching technique alone corresponding to the changes in hepatic shape following breath-holding. In fact, some improvement was seen at the periphery of the liver on temporal and dynamic subtraction images with the new technique.

The present arterial-phase and nonenhanced CT images of the upper abdominal region were obtained during a single breath-hold on CT examination. The dynamic subtraction images with this new technique showed perfect registration on the global hepatic region and improvement on the periphery of the liver (Fig. 5). The image quality on dynamic subtraction images was improved in the lower hepatic region. The 3D nonlinear image-warping technique used template VOIs and the corresponding search-area VOIs, which contained useful information for image matching, including the hepatic region and other organs, such as the kidney and spleen surrounding the hepatic region. In addition, nonenhanced CT was performed first and began at the top of the liver in the craniocaudal

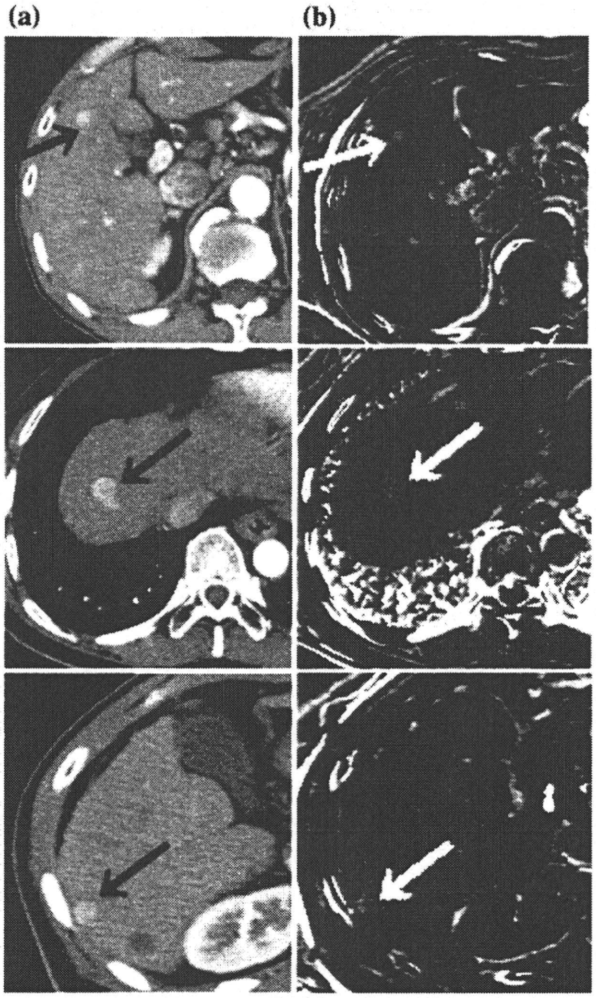

Fig. 9 Comparison of **a** present arterial-phase CT images and **b** temporal subtraction images with the new technique for deformation of HCC

direction. After acquisition of nonenhanced liver images, arterial-phase CT was performed continuously with contrast medium. Therefore, we assumed that temporal deformation and movement between present arterial-phase CT images and nonenhanced CT images was decreased.

However, in comparison with dynamic subtraction images, it may be difficult automatically to select images from the same anatomic positions of the hepatic region between present and previous arterial-phase CT images during a single breath-hold. Therefore, misregistration errors appeared in temporal subtraction images in one case of 3D hepatic region deformation (Fig. 7). In this study, we assumed that movement and deformation in the AP, LR, and SI directions ranged over a maximum of 12 cm in the hepatic region between present and previous arterial-phase CT images during a single breath-hold [28]. We assumed that this range of movement and deformation was adapted to the search area VOIs (8.8 × 8.8 × 8.8 cm; matrix sizes) where the 3D nonlinear image-warping technique was used. Figure 9 shows deformation of HCC on (a) present nonenhanced CT images and (b) temporal subtraction images with the new technique. In 3D nonlinear image warping, the shift vectors with the B-spline curve were smoothed to reduce misregistration errors. Therefore, on present nonenhanced CT images (Fig. 9a) and temporal subtraction images (Fig. 9b), deformation of HCC was markedly unchanged. To our knowledge, there have been no previous reports of deformation of nodules in temporal subtraction techniques with chest CT images and chest radiographs [20–26].

5 Conclusions

We developed a new temporal and dynamic subtraction technique based on the 3D global-matching plus 3D image-warping technique. The quality of the temporal and dynamic subtraction images was improved considerably by this new method. This method may be useful with CT images for improvement of the diagnostic performance in the detection of enhanced nodules.

References

1. Brancatelli G, Baron RL, Peterson MS, Marsh W. Helical CT screening for hepatocellular carcinoma in patients with cirrhosis: frequency and causes of false-positive interpretation. Am J Roentgenol. 2003;180(4):1007–14.
2. el-Serag HB. Epidemiology of hepatocellular carcinoma. Clin Liver Dis. 2001;5:87–107.
3. Schafer DF, Sorrell MF. Hepatocellular carcinoma. Lancet. 1999; 353:1253–7.
4. Baron RL, Peterson MS. Screening the cirrhotic liver for hepatocellular carcinoma with CT and MRI imaging. Radiographics. 2001;21:117–32.
5. Peterson MS, Baron RL, Marsh JW, Oliver JH, Confer SR, Hunt LE. Pretransplantation surveillance for possible hepatocellular carcinoma in patients with cirrhosis: epidemiology and CT-based tumor detection rate in 430 cases with surgical pathologic correlation. Radiology. 2000;217:743–9.
6. Krinsky GA, Lee VS, Theise ND, Weinreb JC, Rofsky NM, Diflo T, Teperman LW. Hepatocellular carcinoma and dysplastic nodules in patients with cirrhosis: prospective diagnosis with MR imaging and explantation correlation. Radiology. 2001;219:445–54.
7. Marin D, Di Martino M, Guerrisi A, De Filippis G, Rossi M, Ginanni Corradini S, Masciangelo R, Catalano C, Passariello R. Hepatocellular carcinoma in patients with cirrhosis: qualitative comparison of gadobenate dimeglumine-enhanced MR imaging and multiphasic 64-section CT. Radiology. 2009;251:85–95.
8. Okumura E, Sanada S, Suzuki M, Matsui O. Computer-aided temporal and dynamic subtraction technique of the liver for detection of small hepatocellular carcinoma on abdominal CT images. Phys Med Biol. 2006;51(19):4759–71.

9. Okumura E, Sanada S, Suzuki M, Takemura A, Matsui O. Improvement of temporal and dynamic subtraction images on abdominal CT using 3D global image matching and nonlinear warping technique. Phys Med Biol. 2007;52(21):6461–74.
10. Rohlfing T, Maurer CR Jr, O'Dell WG, Zhong J. Modeling liver motion and deformation during the respiratory cycle using intensity-based nonrigid registration of gated MR images. Med Phys. 2004;31(3):427–32.
11. Stancanello J, Berna E, Cavedon C, Francescon P, Loeckx D, Cerveri P, Ferrigno G, Baselli G. Preliminary study on the use of nonrigid registration for thoraco-abdominal radiosurgery. Med Phys. 2005;32(12):3777–85.
12. Christina Lee WC, Tublin ME, Chapman BE. Registration of MR and CT images of the liver: comparison of voxel similarity and surface based registration algorithms. Comput Methods Programs Biomed. 2005;78(2):101–14.
13. Brock KM, Balter JM, Dawson LA, Kessler ML, Meyer CR. Automated generation of a four-dimensional model of the liver using warping and mutual information. Med Phys. 2003;30(6):1128–33.
14. Pevsner A, Davis B, Joshi S, Hertanto A, Mechalakos J, Yorke E, Rosenzweig K, Nehmeh S, Erdi YE, Humm JL, Larson S, Ling CC, Mageras GS. Evaluation of an automated deformable image matching method for quantifying lung motion in respiration-correlated CT images. Med Phys. 2006;33(2):369–76.
15. Coselmon MM, Balter JM, McShan DL, Kessler ML. Mutual information based CT registration of the lung at exhale and inhale breathing states using thin-plate splines. Med Phys. 2004;31(11):2942–8.
16. Söhn M, Birkner M, Chi Y, Wang J, Di Y, Berger B, Alber M. Model-independent, multimodality deformable image registration by local matching of anatomical features and minimization of elastic energy. Med Phys. 2008;35(3):866–78.
17. Sarrut DZ. Deformable registration for image-guided radiation therapy. Med Phys. 2006;16(4):285–97.
18. McInerney T, Terzopoulos D. Deformable models in medical image analysis: a survey. Med Image Anal. 1996;1(2):91–108.
19. Hutton BF, Braun M, Thurfjell L, Lau DY. Image registration: an essential tool for nuclear medicine. Eur J Nucl Med Mol Imaging. 2002;29(4):559–77.
20. Kano A, Doi K, MacMahon H, Hassell DD, Giger ML. Digital image subtraction of temporally sequential chest images for detection of interval change. Med Phys. 1994;21(3):453–61.
21. Ishida T, Katsuragawa S, Nakamura K, MacMahon H, Doi K. Iterative image warping technique for temporal subtraction of sequential chest radiographs to detect interval change. Med Phys. 1999;26(7):1320–9.
22. Li Q, Katsuragawa S, Ishida T, Yoshida H, Tsukkuda S, MacMahon H, Doi K. Contralateral subtraction: a novel technique for detection of asymmetric abnormalities on digital chest radiography. Med Phys. 2000;27(1):47–55.
23. Li Q, Katsuragawa S, Doi K. Improved contralateral subtraction images by use of elastic matching technique. Med Phys. 2000;27(6):1934–42.
24. Abe H, Ishida T, Shiraishi J, Li F, Katsuragawa S, Sone S, MacMahon H, Doi K. Effect of temporal subtraction images on radiologists' detection of lung cancer on CT: result of the observer performance study with use of file computed tomography images. Acad Radiol. 2004;11:1337–43.
25. Takao H, Doi I, Watanabe T, Tateno M. Temporal subtraction of thin-section thoracic computed tomography based on a 3-dimensional nonlinear geometric warping technique. J Comput Assist Tomogr. 2006;30(2):283–6.
26. Takao H, Doi I, Takeno M. Evaluation of an automated system for temporal subtraction of thin-section thoracic CT. Br J Radiol. 2007;80(950):85–9.
27. Oguro S, Tokuda J, Elhawary H, Haker S, Kikinis R, Tempany CM, Hata N. MRI signal intensity based B-spline nonrigid registration for pre- and intraoperative imaging during prostate brachytherapy. J Magn Reson Imaging. 2009;30(5):1052–8.
28. Nguyen TN, Moseley JL, Dawson LA, Jaffray DA, Brock KK. Adapting liver motion models using a navigator channel technique. Med Phys. 2009;36(4):1061–73.
29. Nguyen TN, Moseley JL, Dawson LA, Jaffray DA, Brock KK. Adapting population liver motion models for individualized online image-guided therapy. Conf Proc IEEE Eng Med Biol Soc. 2008;2008:3945–8.
30. Brock KK, Hollister SJ, Dawson LA, Balter JM. Creating a four-dimensional model of the liver using finite element analysis. Med Phys. 2002;29(7):1403–5.
31. Brock KK, Sharpe MB, Dawson LA, Kim SM, Jaffray DA. Accuracy of finite element module-based multi-organ deformable image registration. Med Phys. 2005;32(6):1647–59.